SUPPLEMENTARY INFORMATION

Thermoelectric Performance Boost by Chemical Order in Epitaxial L2_1 (100) and (110) Oriented undoped Fe2VAl Thin Films: An Experimental and Theoretical Study

José María Domínguez-Vázquez[a], Olga Caballero-Calero[a], Ketan Lohani[a], José J. Plata[b], Antonio M. Marquez[b], Cristina V. Manzano[a], Miguel Ángel Tenaguillo[a], Hiromichi Ohta[c], Alfonso Cebollada[a], Andres Conca[a,*], and Marisol Martín-González[a].

[a]Instituto de Micro y Nanotecnología, IMN-CNM, CSIC (CEI UAM+CSIC), Isaac Newton 8, E-28760 Tres Cantos, Madrid, Spain
[b]Dpto de Química Física, Facultad de Química, Universidad de Sevilla, Sevilla (Spain).
[c]Research Institute for Electronic Science, Hokkaido University, N20W10, Kita, Sapporo, 001–0020, Japan.
*Corresponding author: andres.conca@csic.es

The complete X-Ray characterization of Fe_2VAl films is portrayed in SI 1, SI 2, SI 3, SI 4, SI 5 and SI 6. In SI 1 and SI 4 the specular measurements (ψ=0°) are portrayed for samples deposited over Al_2O_3 and MgO, respectively. These measurements are presented for the whole array of deposition temperatures (T_{dep}). In these figures is more visible the single-oriented nature of films deposited over MgO and polycrystalline to single-oriented transition of the ones deposited over Al_2O_3, as it was mentioned in the main text. MgO substrate films show the (2 0 0) X-Ray diffraction spot, meaning this that the B2 phase is present on all samples, while Al_2O_3 substrate ones show this feature for samples deposited at 750 °C or higher. The (1 1 1) diffraction peak, associated with L2_1 phase, is present for Fe_2VAl films deposited either on Al_2O_3 or MgO at T_{dep} of 850 °C or higher, as it is depicted in SI 3 and SI 6.

Another structural factor that influences thermal and transport behavior of thin films is their in-plane registry with the substrate and crystallite dispersion. We delve into it by performing ϕ–scans of asymmetric diffraction reflections of both layer and substrate (Schematic of the measurement configuration is shown in the inset to the SI 7 (a)). In SI 7 b) and c), we show ϕ–scans for the Fe_2VAl (2 2 0) and (4 0 0) peaks on both substates deposited at 950 °C. For the MgO substrate, the Fe_2VAl (2 2 0) scan is plotted together with MgO (2 2 0), demonstrating that Fe_2VAl grows epitaxially with a 45° in-plane rotation relative to the lattice axis of MgO (see schematic in SI 7 d)). This rotation corresponds to the epitaxial relation $[1\ 0\ 0]_{Fe_2VAl}//[1\ 1\ 0]_{MgO}$ and minimizes the lattice mismatch between layer and substrate. It is worth mentioning this has been previously observed in other full Heusler systems grown on MgO with similar lattice constant [1]. Lattice parameter of MgO is 0.4213 nm, while the nominal lattice parameter of Fe_2VAl is 0.5763 nm. Therefore, at 45°, the calculated lattice mismatch is $\frac{(a_{Fe_2VAl} - \sqrt{2}\cdot a_{MgO})}{(\sqrt{2}\cdot a_{MgO})} =$ 3.3%. This epitaxial growth occurs for deposition temperatures of 350 °C or higher.

For the Al_2O_3 substrate, the ϕ–scan of Fe_2VAl (4 0 0) peak is shown together with the Al_2O_3 (1 1 $\bar{2}$ 0) in SI 7 c) for the film grown at 950 °C. Here, a two-fold rotation symmetry is expected for both reflections. However, a more complex behavior is observed due to a collection of peaks originating from the layer, in addition to those from the substrate. The schematic in SI 7 d) allows identifying the different relative in-plane orientations of the different film's crystallites grown on top of the substrate. As illustrated, there is a major orientation, a secondary orientation, and one minor orientation, identified by the blue, green, and yellow arrows, respectively. The epitaxial ratio corresponding to major and secondary orientation is $[1\ 1\ 0]_{Fe_2VAl}//[0\ 0\ 1]_{Al_2O_3}$ and $[1\ 0\ 0]_{Fe_2VAl}//[0\ 0\ 1]_{Al_2O_3}$, respectively. For the preferential orientation case (blue arrows), the Al_2O_3 lattice parameter relevant for this orientation is c(Al_2O_3) =1.2993 nm. This corresponds to a mismatch of $(\frac{2}{3}c(Al_2O_3) - \sqrt{2}\cdot a(Fe_2VAl))/(\frac{2}{3}c(Al_2O_3)) =$ 5.9%. On the other hand, for the secondary orientation (green arrows), the relevant lattice parameter is *a*(Al_2O_3) = 0.4760 nm, resulting in a mismatch of $((1.5\cdot\frac{a(Al_2O_3)}{cos(30)} - \sqrt{2}\cdot a(Fe_2VAl))/(1.5\cdot\frac{a(Al_2O_3)}{cos(30)}) =$ 14.4%. Thus, the preferred orientation of the lattice can be explained by the smaller mismatch with respect to the substrate. Every lattice parameter and correspondent mismatch is summarized in Table 1.

	Subs. Lattice parameters	**Lattice mismatch**
a (Fe_2VAl) =0.5763 nm	a (MgO) = 0.4213 nm	3.3% $[1\,0\,0]_{Fe_2VAl}//[1\,1\,0]_{MgO}$
	a (Al_2O_3) =0.4760 nm c (Al_2O_3) = 1.2993 nm	14.4% $[1\,0\,0]_{Fe_2VAl}//[0\,0\,1]_{Al_2O_3}$ 5.9% $[1\,1\,0]_{Fe_2VAl}//[0\,0\,1]_{Al_2O_3}$

Table 1: Lattice parameters of Fe_2VAl and substrates and the obtained lattice mismatch for each orientation.

This behavior has previously been reported for another full Heusler alloy with a similar lattice constant but different composition, $Co_2Cr_{0.6}Fe_{0.4}Al$, pointing to a general trend with these materials and substrates [2,3]. Films deposited on Al_2O_3, for temperatures below 850 °C yield featureless, non-zero signal, ϕ-scans, indicating a complete in-plane disorder although they are still out-of-plane single-oriented for T_{dep} above 800 °C.

In SI 8 a series of ϕ-scans of the (2 2 0) diffraction peak at several T_{dep} of Fe_2VAl thin films is shown, a four-fold rotation is observed for all samples, proving epitaxial growth for the whole series. On the other hand, in SI 9, a plot of the FWHM of one of the ϕ-scan peaks is portrayed. In this figure one can see the decay of the FWHM when higher T_{dep} are applied, which implies a higher in-plane order of the crystallites.

For films deposited over Al_2O_3 SI 10 shows ϕ-scans of the (4 0 0) diffraction peak at T_{dep} from 800 °C to 950 °C, for lower T_{dep} this plot is featureless. For T_{dep} of 850 and 900 °C two preferential orientations are observed, explained in the main text, while at 950 °C the orientation $[1\ 1\ 0]_{Fe_2VAl}//[0\ 0\ 1]_{Al_2O_3}$ (peaks at $\phi=90^o$ and 270^o) shows higher intensity.

Furthermore, to complete the information about the crystal characteristics and regain insight on lattice distortions present in the films, we have calculated the lattice interplanar distances. In SI 11, we show the dependence of the out-of-plane interplanar distances on T_{dep}, measured and projected from specular (ψ=0°) and off-specular (ψ=45°) XRD measurements, for films grown on MgO and Al_2O_3, respectively. This plot allows to distinguish whether the crystal structure presents a deformation from an expected cubic structure. For a perfectly cubic crystal structure, the interplanar distance of each (*h, k, l*) family of planes is defined by $d_{h,k,l} = \frac{a}{\sqrt{h^2+k^2+l^2}}$, and $a = d_{1\,0\,0} = 4\cdot d_{4\,0\,0} = 2\cdot d_{2\,0\,0} = \sqrt{8}\cdot d_{2\,0\,0}$, thus a difference between the last three quantities, $4\cdot d_{4\,0\,0}$ or $2\cdot d_{2\,0\,0}$and $\sqrt{8}\cdot d_{2\,0\,0}$ is a proof of non-isotropic distortion of the lattice. For comparison reasons, in SI 11 , the interplanar distances are plotted together with the reported bulk lattice parameter obtained from[4]. SI 11 b), depicts in-plane interplanar distances for the three highest T_{dep} due to the absence of (*h* 0 0) peaks for lower temperature cases. For both substrates, the increasing T_{dep} results in a decrease in the lattice parameter, reaching values close to the ones reported on bulk samples, particularly for films deposited on Al_2O_3, where the difference is less than $2\cdot10^{-3}$nm. Lattice parameter and crystallite size extracted from Rietveld analysis, and their dependence on T_{dep}, are shown in the SI. In brief, the crystallite size (in the order of 20 nm) gradually increases with increasing growth temperature, as expected in these kinds of thin films.

To complete the information about the crystal characteristics of these films, in SI 12 we show the growth temperature dependence out-of-plane crystallite size for both layer orientations obtained from Rietveld analysis of the symmetrical and asymmetrical XRD $\theta/2\theta$ scans. As it can be seen, the out-of-plane crystallite size gradually increase with increasing T_{dep}, which is the usual behavior in thin film growth, films grown on MgO appear to have a tendency to increase faster with T_{dep} than the ones deposited over Al_2O_3.

In addition to electronic transport and thermoelectric properties, charge carrier concentration was measured in all samples and is included in SI 13, although the thin nature of the films affects the quality of the measurements, making it impossible to differentiate the concentration between samples. However, all the measured values are in the range of 10^{20}cm^{-3}. Scanning electron microscope (SEM) images of all samples are shown in SI 14 and SI 15, the former showing Fe_2VAl deposited over Al_2O_3 and the latter over MgO. AFM measurements were performed on samples deposited at 550 and 850 °C over the two substrates and are shown in SI 16 and SI 17, where it is visible on the profiles at the right of the images that the surface roughness increases significantly with T_{dep}. Also, extracted values of RMS are shown in Table 2.

The calculated thermal properties of Fe_2VAl is summarized in SI 18, where dispersion curves and group velocities are calculated for the $L2_1$ phase. SI 18 c) portraits the scattering rates of chemically ordered $L2_1$ Fe_2VAl, along with the cases where 6% and 15% chemical disorder were simulated. In SI 18 d) the calculated lattice thermal conductivity is plotted along with the estimated values obtained on two measured samples. This estimation was made subtracting the electronic contribution, obtained with the Wiedemann-Franz law ($\kappa_e = \sigma \mathrm{LT}$)[5] using a Lorenz number of $L=2.4\cdot10^{-8}\ V^2K^{-2}$, to the total thermal conductivity measured with TDTR.

The thermoelectric properties dependence on carrier concentration and crystallite size is shown in SI 19 as a form of heat maps.

The optical band gap measurement done with Tauc plot is shown in SI 20, this measurement gives the same result as the Pankove plot shown in the main text (E_g=0.19±0.05 eV).

Substrate	T_{dep} (^oC)	RMS (nm)
MgO	550	0.57
	850	3.95
Al_2O_3	550	1.17
	850	3.98

Table 2: Root Mean Square (RMS) roughness values obtained for samples deposited at 550 and 850^{o}C over Al_2O_3 and MgO.

XRD

Al_2O_3 substrate:

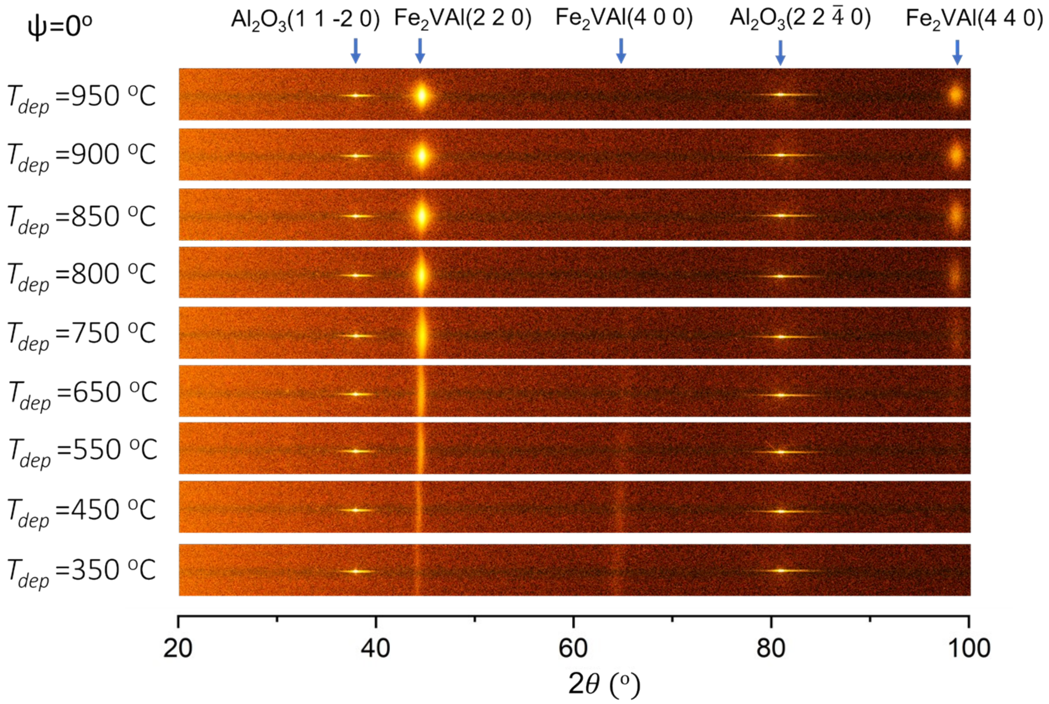

SI 1: specular (ψ=0°) X-Ray $\theta/2\theta$ vs γ 2D maps for Fe_2VAl films at all deposition temperatures (T_{dep}) deposited over Al_2O_3 substrate.

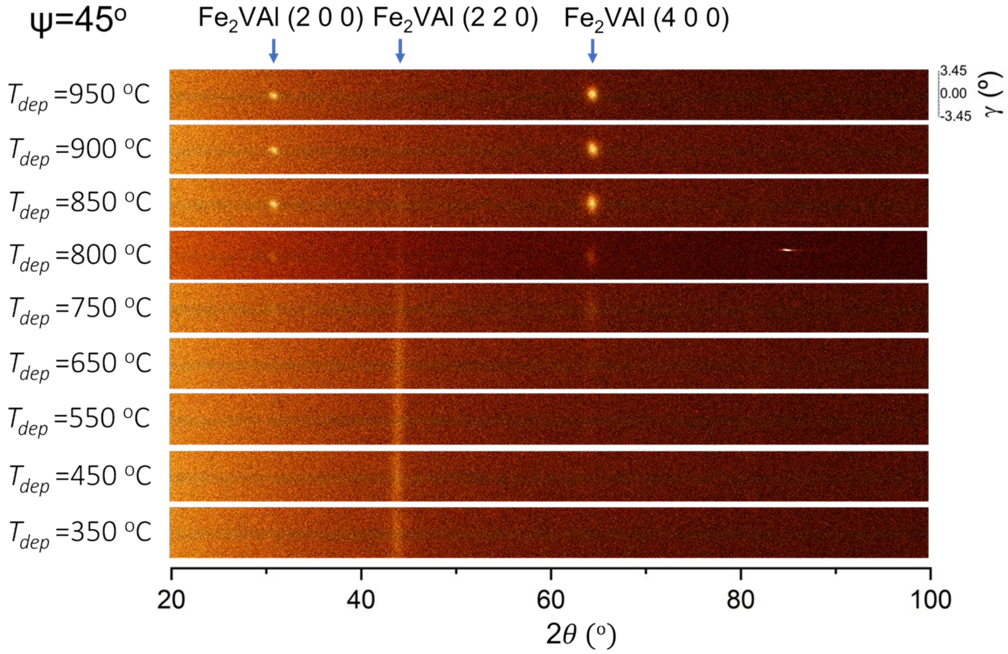

SI 2: Off-specular (ψ=45°) X-Ray $\theta/2\theta$ vs γ 2D maps for Fe_2VAl films at all deposition temperatures (T_{dep}) deposited over Al_2O_3 substrate.

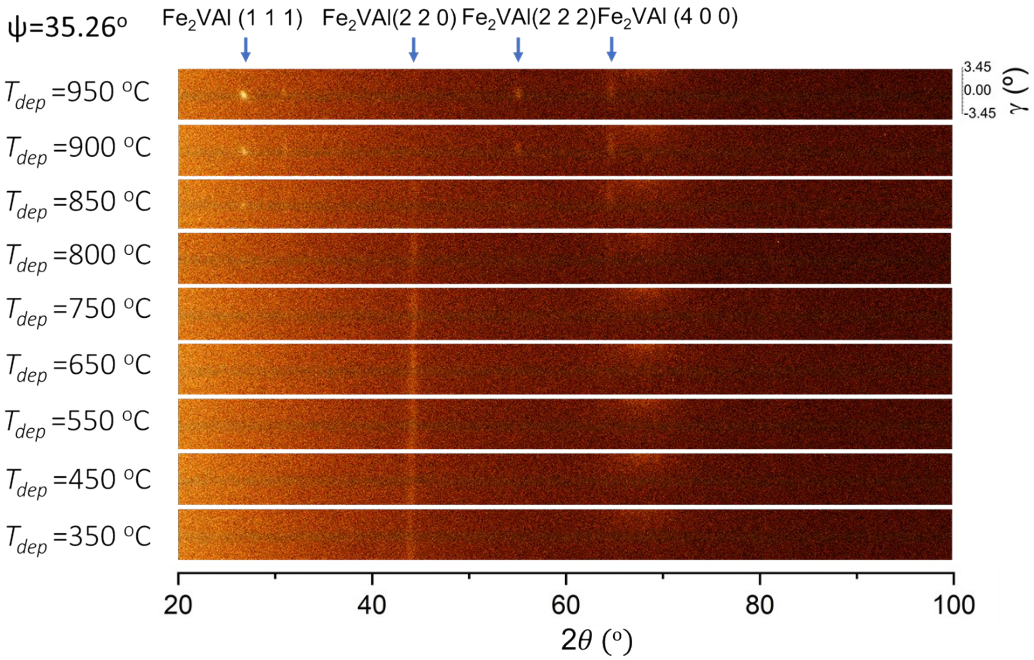

SI 3: Off-specular (ψ=35.26°) X-Ray $\theta/2\theta$ vs γ 2D maps for Fe_2VAl films at all deposition temperatures (T_{dep}) deposited over Al_2O_3 substrate.

MgO substrate:

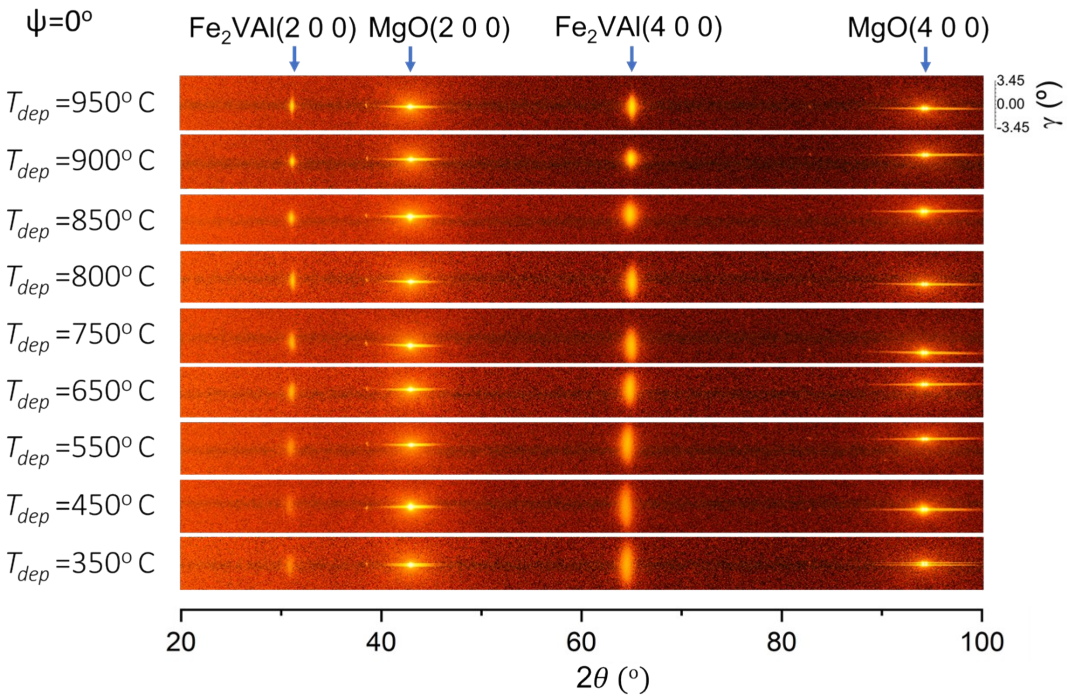

SI 4: specular (ψ=0°) X-Ray $\theta/2\theta$ vs γ 2D maps for Fe_2VAl films at all deposition temperatures (T_{dep}) deposited over MgO substrate.

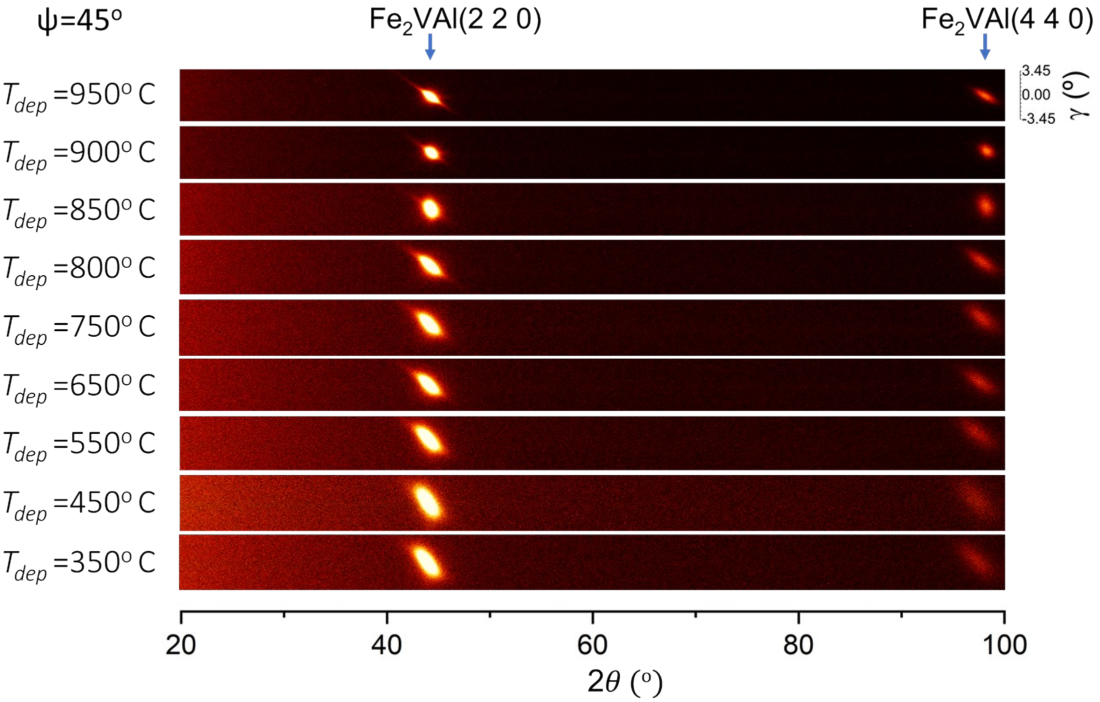

SI 5: Off-specular (ψ=45°) X-Ray $\theta/2\theta$ vs γ 2D maps for Fe_2VAl films at all deposition temperatures (T_{dep}) deposited over MgO substrate.

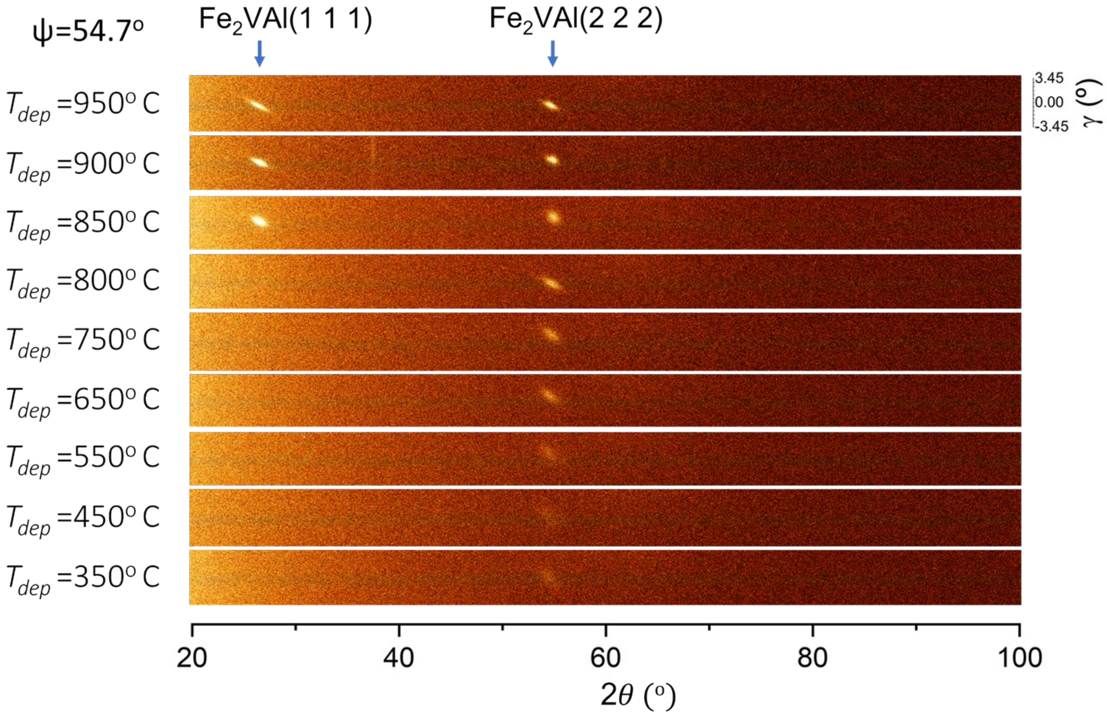

SI 6: Off-specular (ψ=54.7º) X-Ray $\theta/2\theta$ vs γ 2D maps for Fe_2VAl films at all deposition temperatures (T_{dep}) deposited over MgO substrate.

Phi scans, interplanar distances and crystallite size

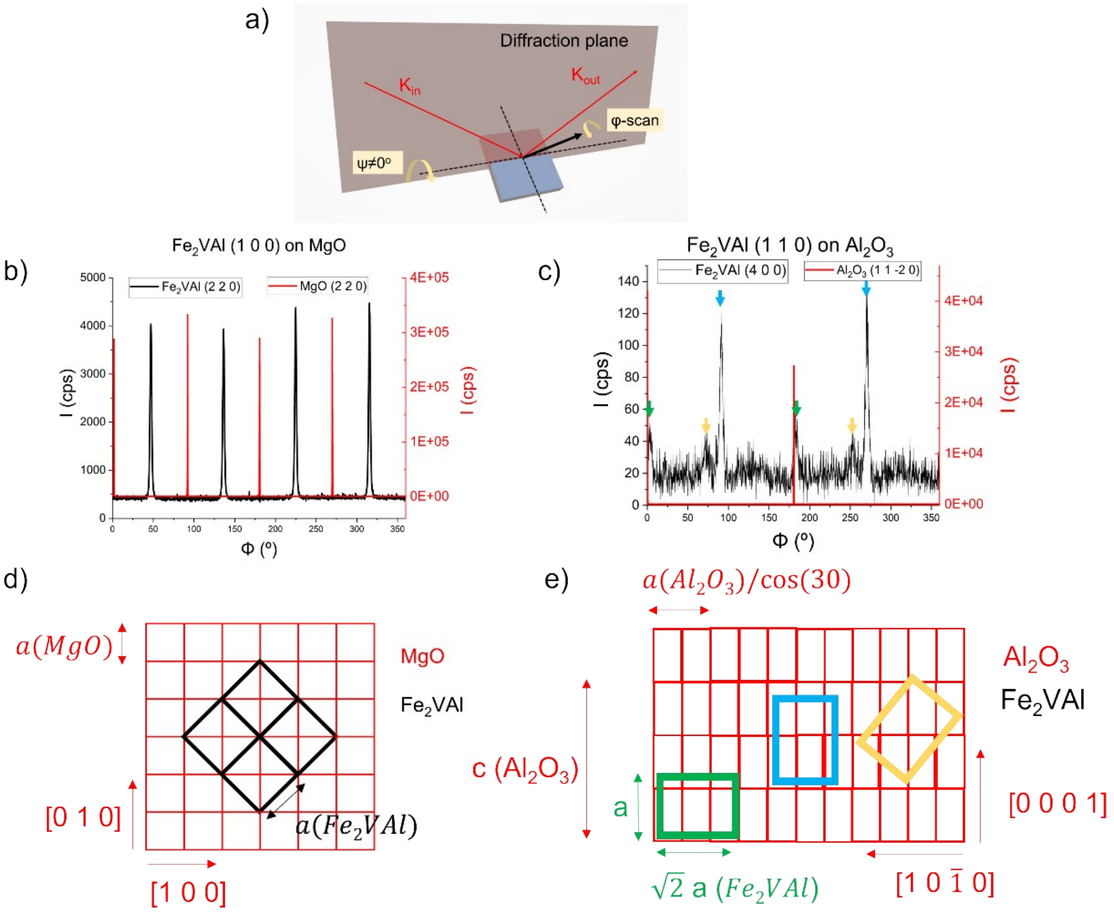

SI 7: ϕ–scans of asymmetrical peaks of Fe_2VAl thin films. a) schematic diagram of the ϕ-scan measurement geometry. For films grown at 850 °C on MgO b) the (2 2 0) peak is plotted and for the ones grown at 950 °C on Al_2O_3 c) the (4 0 0). d) and e) are schematic of the in-plane texture of the films based on the ϕ–scans showed on b) and c), respectively.

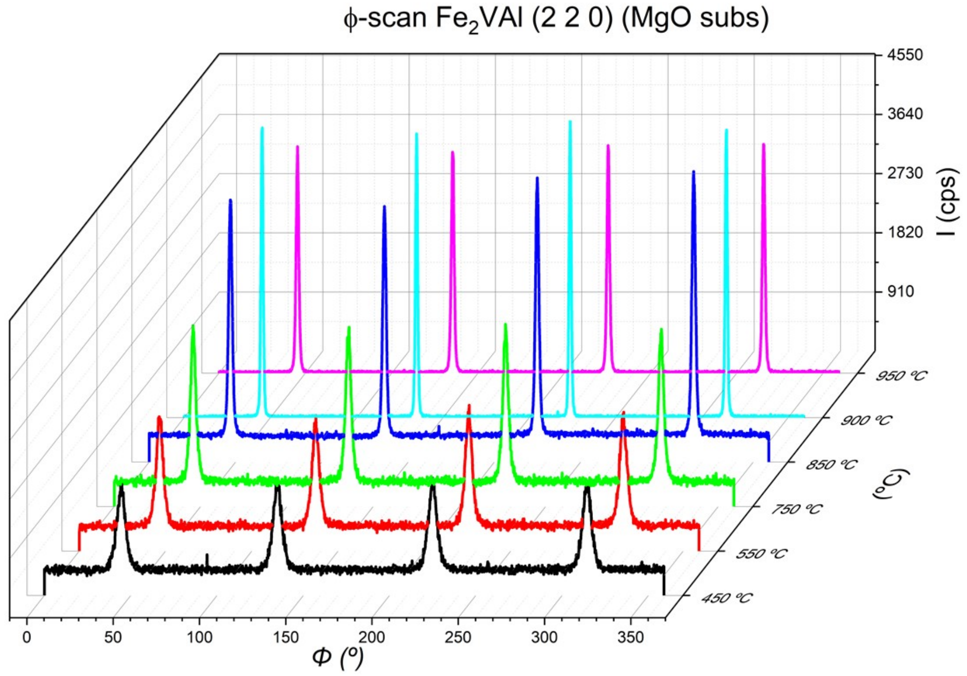

SI 8: ϕ-scan of (2 2 0) diffraction peak of Fe_2VAl films deposited over MgO for various $T_{dep.}$

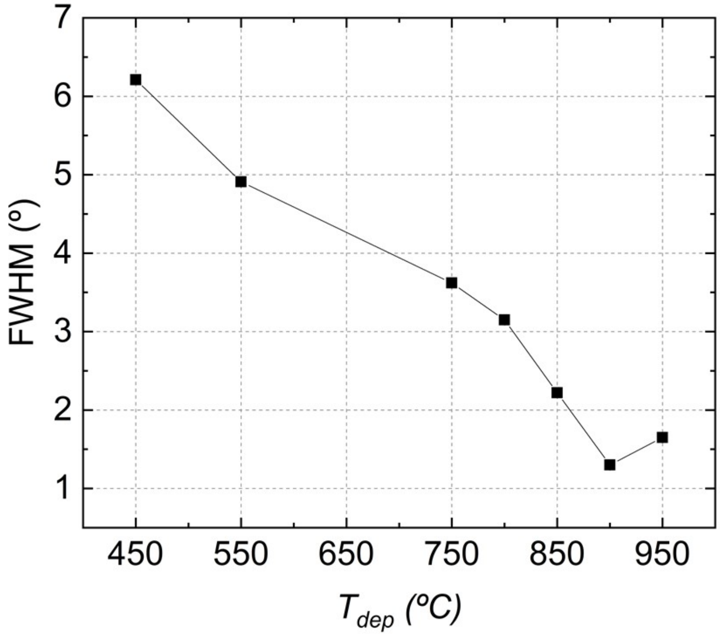

SI 9: Full Width Half Maximum (FWHM) of ϕ-scan peaks of Fe_2VAl films deposited over MgO for various $T_{dep.}$

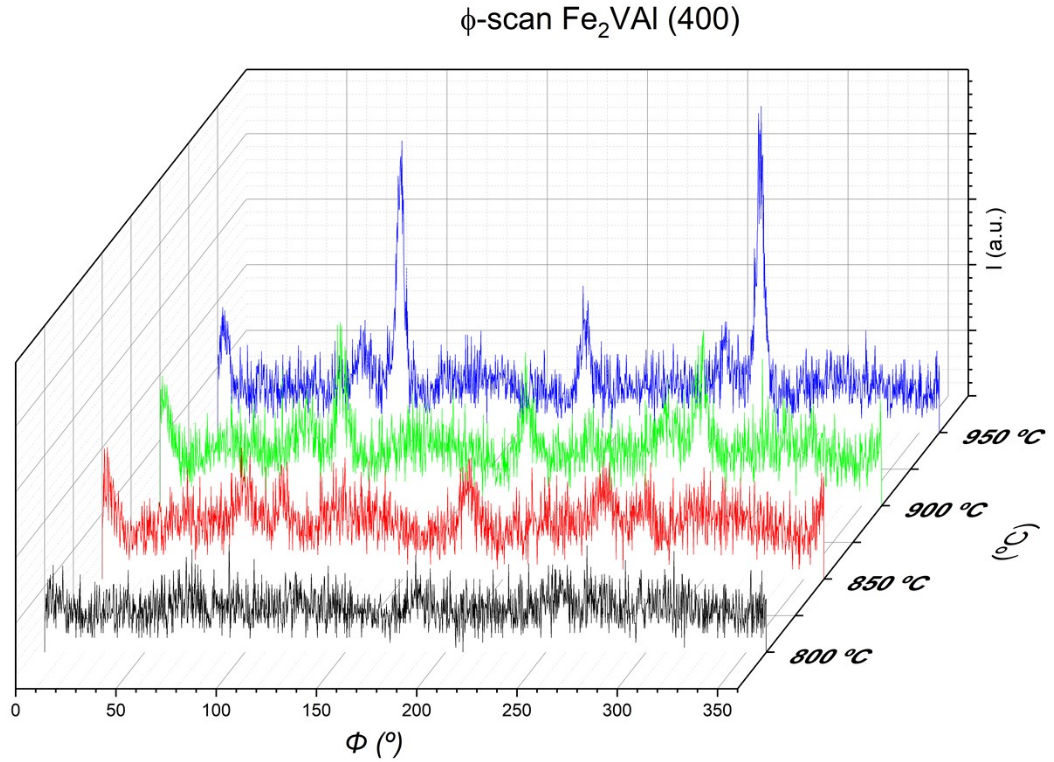

SI 10: ϕ-scan of (4 0 0) diffraction peak of Fe_2VAl films deposited over Al_2O_3 for various $T_{dep.}$

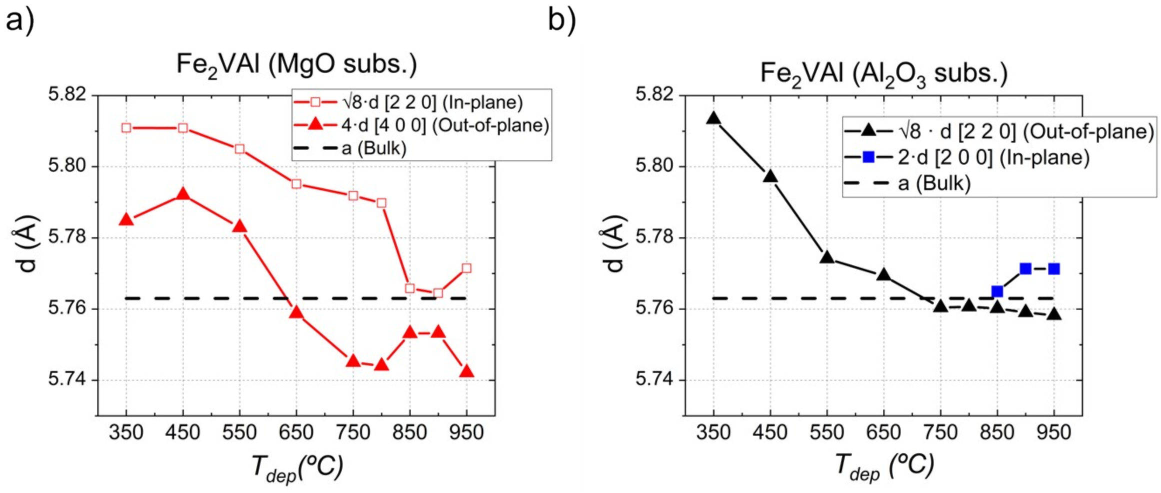

SI 11: Measured out-of-plane ($\psi=0^o$, triangle markers) and in-plane ($\psi=45^o$, square markers) interplanar distances of Fe_2VAl deposited on MgO a), and Al_2O_3 b). The interplanar distances were compared to estimate the deviation of the lattice from a cubic crystal structure, as in this type of crystal structure $a = 4 \cdot d_{4\,0\,0} = 2 \cdot d_{2\,0\,0} = \sqrt{8} \cdot d_{2\,2\,0}$. The measured distances are compared with the bulk lattice parameter of Fe_2VAl from [4].

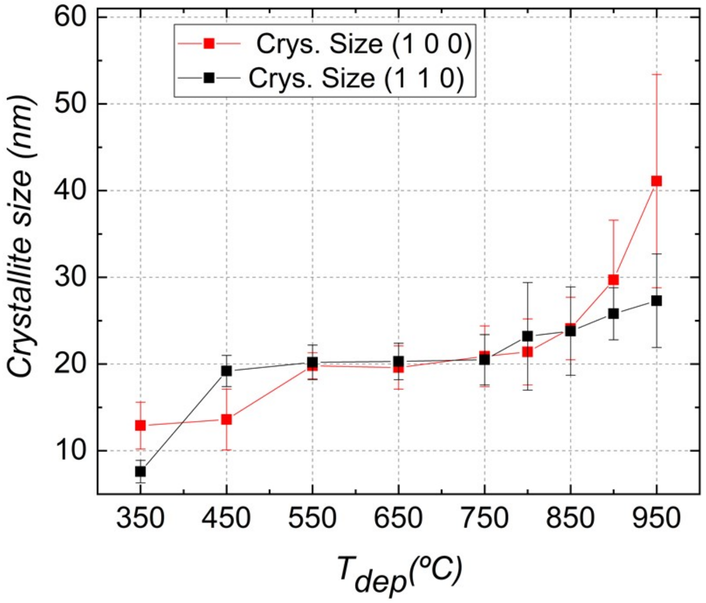

SI 12: Out-of-plane crystallite size obtained from Rietveld analysis of the specular (ψ=0º) θ/2θ measurements of Fe_2VAl (1 0 0) and (1 1 0) films.

Carrier concentration

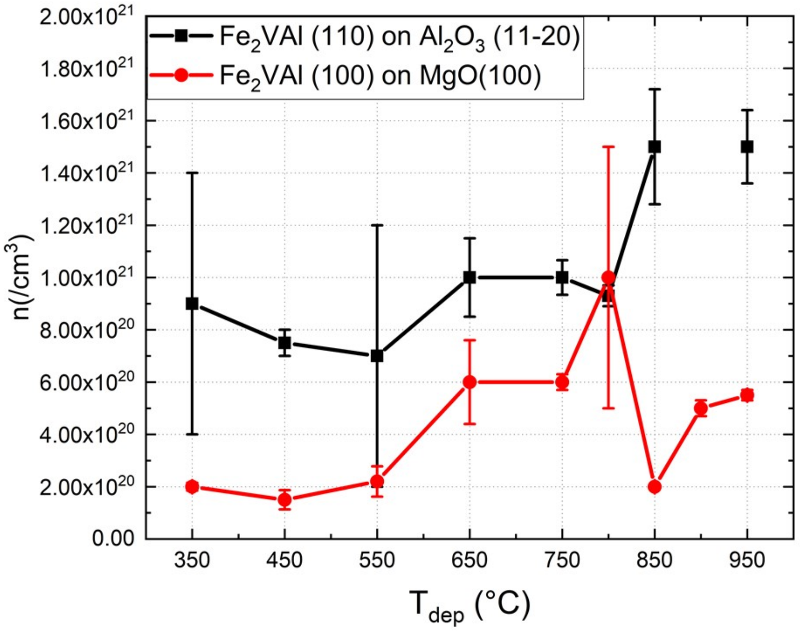

SI 13: Measured Carrier concentration of the Fe_2VAl (1 1 0) and (1 0 0) films deposited at different deposition temperatures.

SEM

Al_2O_3 substrate:

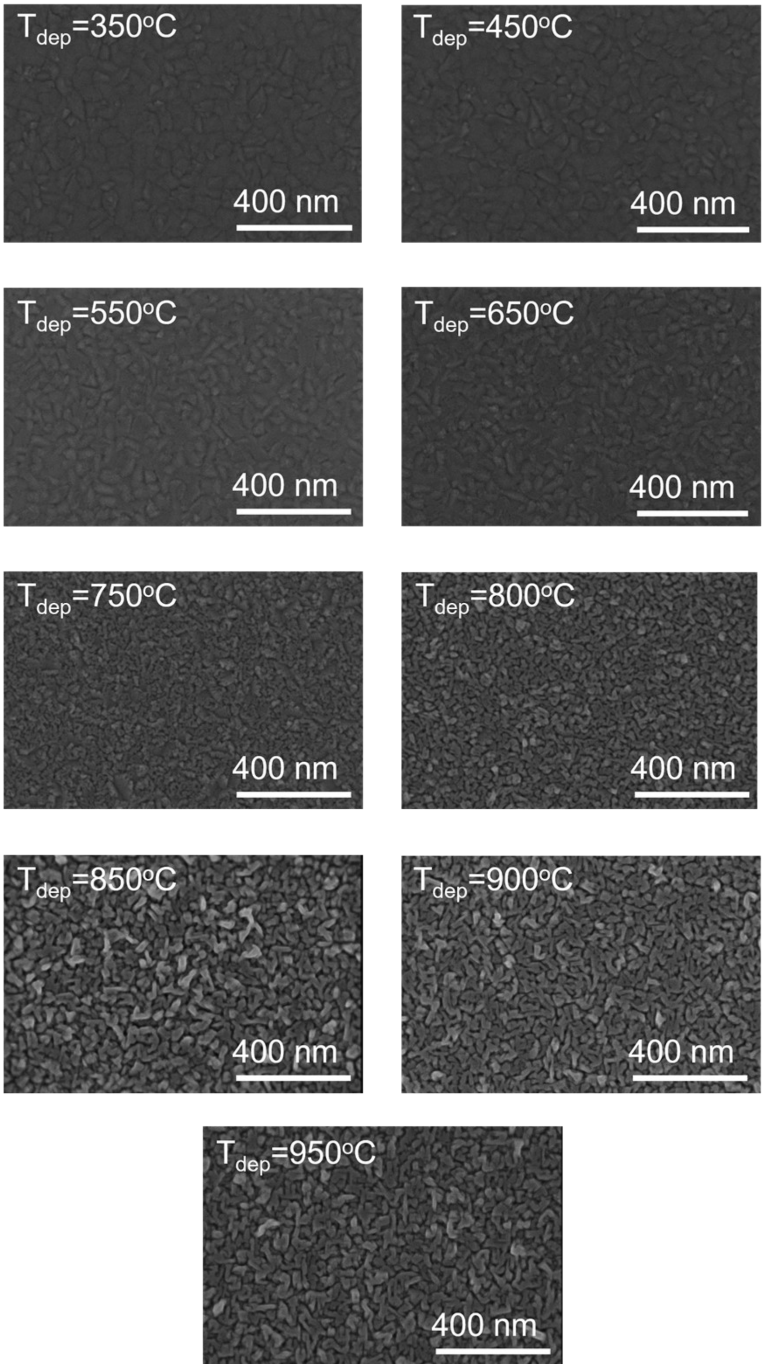

SI 14: SEM images of Fe_2VAl films deposited over Al_2O_3 at all T_{dep}.

MgO substrate:

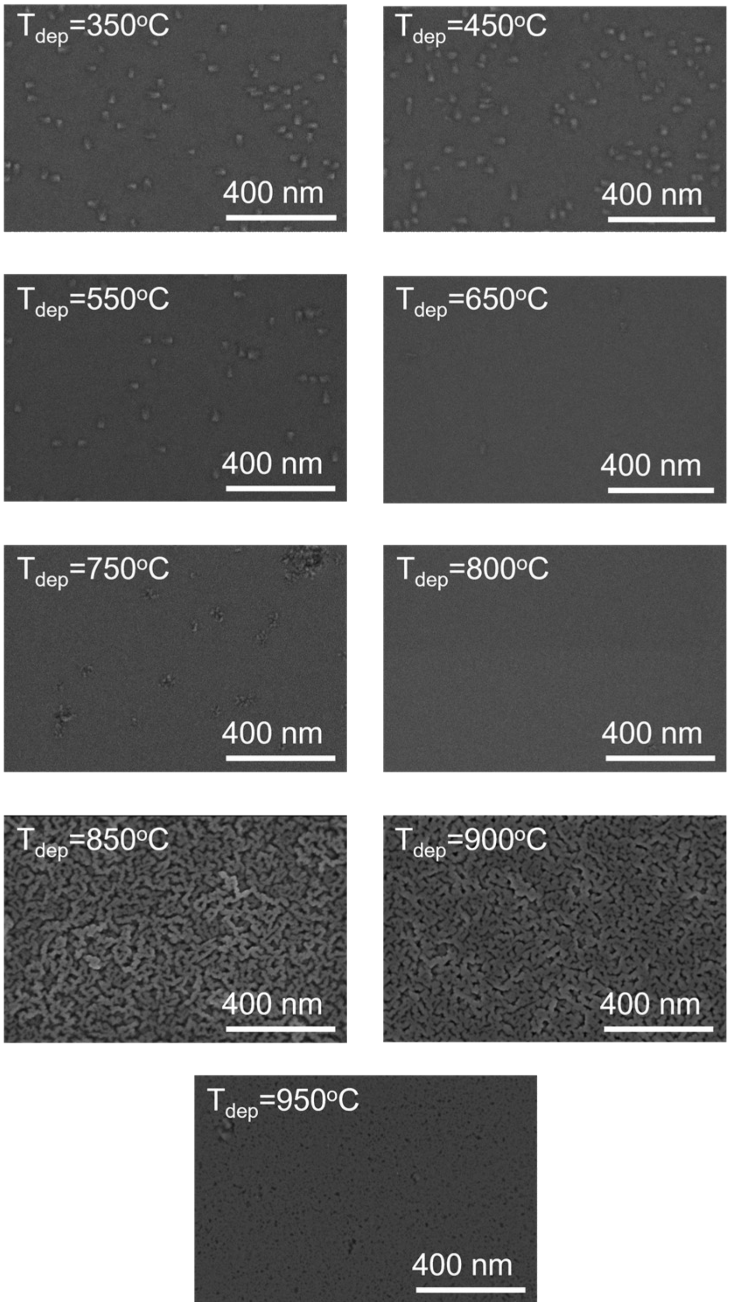

SI 15: SEM images of Fe_2VAl *films deposited over MgO at all* T_{dep}.

AFM

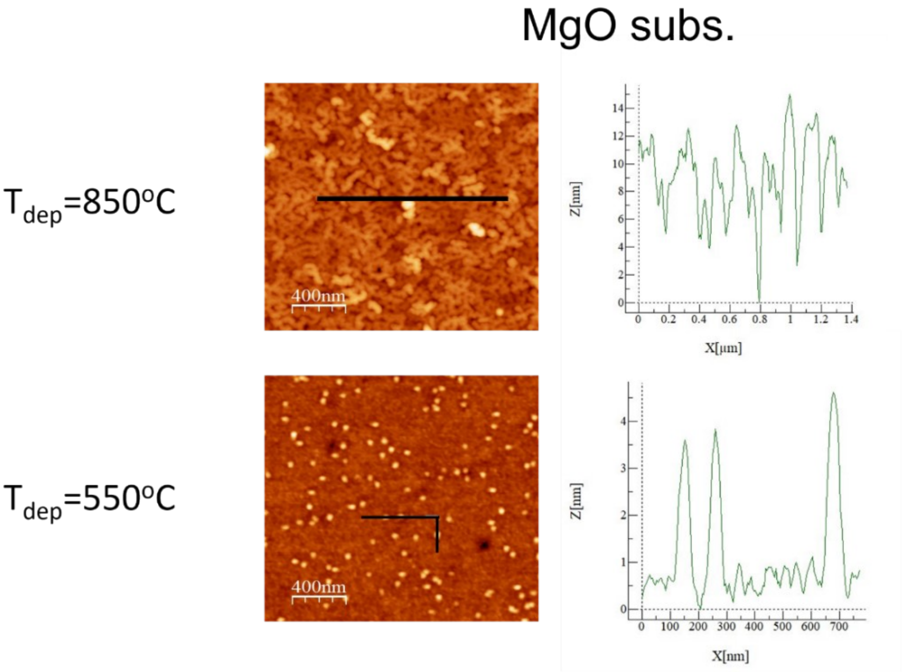

SI 16: AFM images and profile for samples deposited at 550 and 850 ^{o}C over MgO.

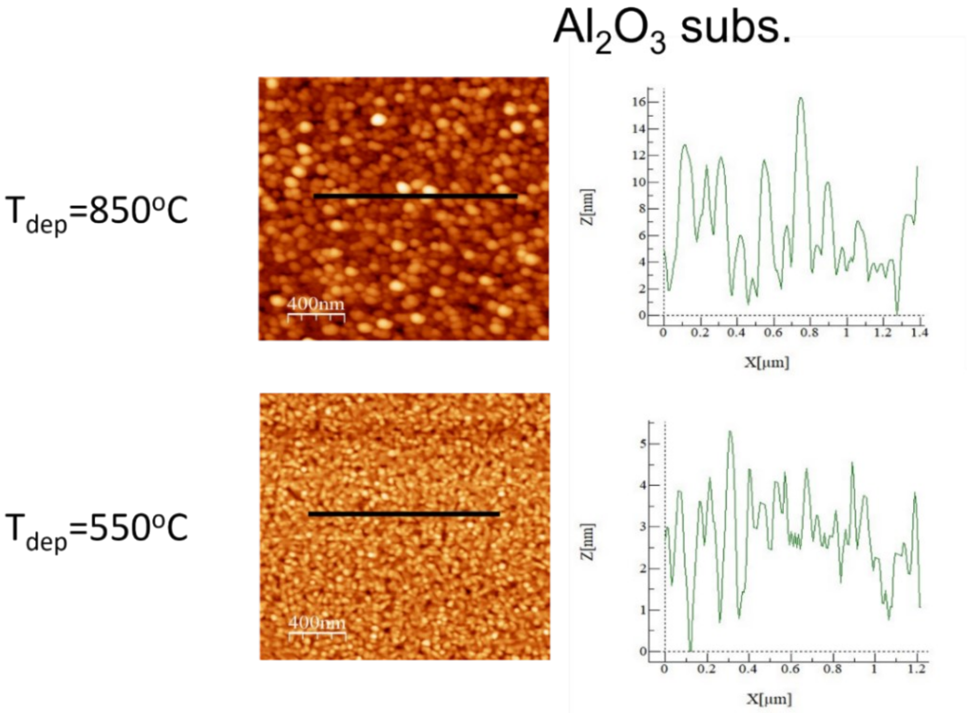

SI 17: AFM images and profile for samples deposited at 550 and 850 ^{o}C over Al_2O_3.

Additional simulations

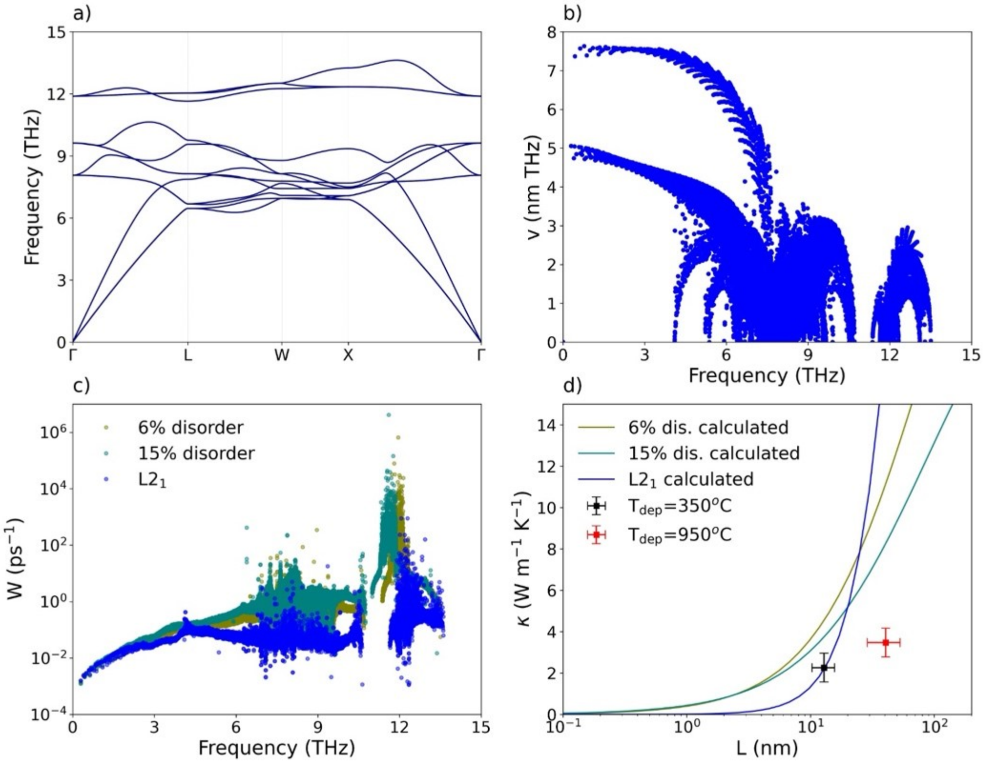

SI 18: a) Dispersion curves and b) group velocities for $L2_1$ phase. c) Scattering rates and d) cumulative thermal conductivity for $L2_1$ phase and disordered systems using Tamura model as a function of the crystallite size.

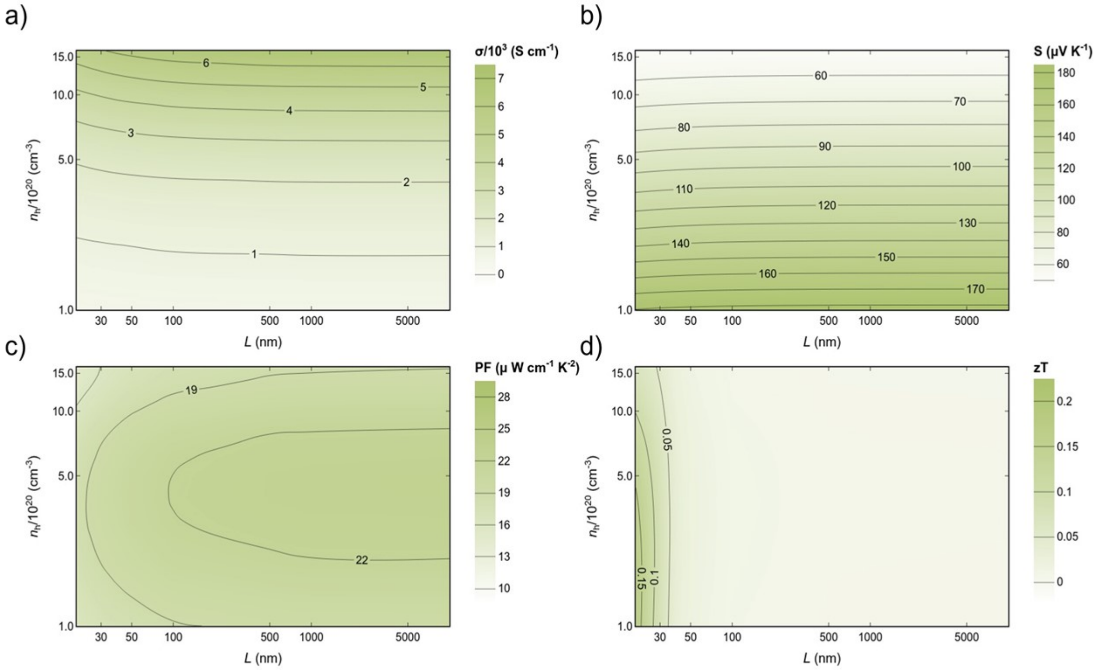

SI 19: Heat maps of a) Electrical conductivity (σ), b) Seebeck coefficient (S), c) Power Factor (PF), and d) thermoelectric figure of merit (zT) dependence on carrier concentration (n) and grain size (L) at 300 K for $L2_1$ Fe_2VAl phase.

There are different factors that can affect the quantitative agreement between experiment and theory. These can be separated into two groups: methodological and modeling limitations.

Methodological limitations: The AMSET code has been proven to accurately describe the electrical transport properties of semiconductors. However, it tends to overestimate them, especially electrical conductivity at high carrier concentrations, as is the case here. At high carrier concentrations, point defects and impurities play a critical role in reducing carrier mobility. These point defects are not explicitly included in our atomic models which may result in an overestimation of the electrical conductivity. This trend has been reported and analyzed in one of our previous works (see J. Santana-Andreo et al.[6]).

Modelling limitations. Including all the experimental variables of the synthesized samples in the theoretical model presents significant computational challenges. We can mention four important factors: carrier concentration, phase coexistence, epitaxial strain, and texture. As shown in Fig SI 19, Seebeck coefficient and electrical conductivity are extremely sensitive to carrier concentration; however, there are large uncertainties in these experimental values. This is why we have selected a range of concentrations for comparing experimental and theoretical values. Further, the calculation assumes full $L2_1$ order. The dominant presence of the $L2_1$ order is confirmed by the strong x-ray diffraction peak, but as is generally known for Heusler compounds, this does not exclude the presence of B2 or A2 phase. In other words, the (111) peak is a proof of the presence of $L2_1$ order but not of the absence of B2 or A2. The presence of some grains in the film with B2/A2 order is not accounted for in the simulation and can potentially contribute to the discrepancy. Regarding texture, while grain size has been included in the calculation of the thermal properties, there are other variables that can play an important role, such as grain morphology or orientation, that are not included in the model. In order to evaluate the effect of the epitaxial strain on the thermoelectric properties, a model in which the lattice parameters have been accordingly modified based on the average in-plane strain reported in Fig S11 has been performed. Under these conditions, we found a 5% reduction of the Seebeck coefficient, which is a small improvement with respect to the strain-free model when compared to the experimental values.

Optical band gap

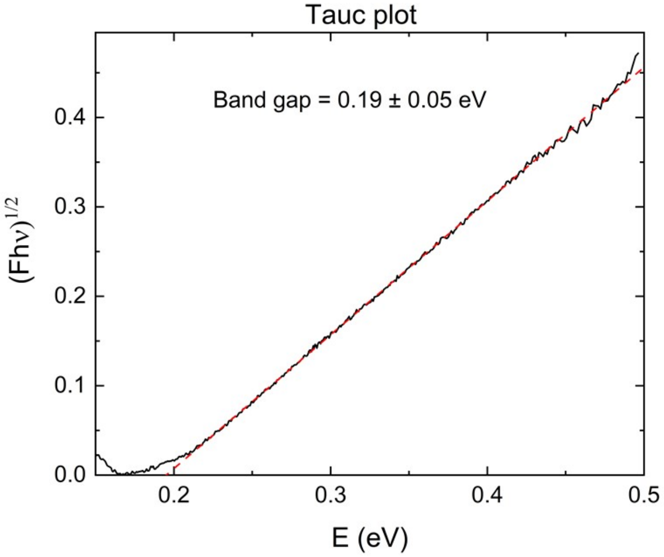

SI 20: Optical measurement of the band gap of Fe_2VAl via Tauc plot. The estimation gives a result of E_g=0.19±0.05 eV.

Reproducibility statements

This work consists of two independently deposited series (on Al_2O_3 and MgO substrates) with deposition temperatures ranging from 350°C to 950°C. In order to avoid temporal drifts in the deposition system each sample series was deposited in a random order of T_{dep} (i.e., chronologically the samples were deposited with T_{dep} covering in a random fashion the T_{dep} range). As it can be seen in Figure 3 in the main text, samples deposited at similar temperatures show similar thermoelectric and electrical properties although they were deposited at different moments. The whole deposition spanned for 5 months, showing the stability of the process. Apart from some minor differences of the thermoelectric values between specific cases of T_{dep}, the general tendency of $L2_1$ boost in the Seebeck coefficient and in the thermoelectric power factor is reproduced. Moreover, the sample for the bandgap determination was deposited more than one month after the two series, since a thicker sample is required for optical measurements (as stated in the main text). Still, the transport properties and thermoelectric values were similar (S~64 μV/ K, PF~467 μW/m·K²). These considerations support the reproducibility and stability of the deposition procedure.

References

1 A. Conca, M. Jourdan, C. Herbort and H. Adrian, *J Cryst Growth*, 2007, 299, 299–302.

2 G. Jakob, F. Casper, V. Beaumont, S. Falk, N. Auth, H. J. Elmers, C. Felser and H. Adrian, *J Magn Magn Mater*, 2005, 290–291, 1104–1107.

3 A. Conca, M. Jourdan and H. Adrian, *J Phys D Appl Phys*, 2007, 40, 1534–1538.

4 Y. Kawaharada, K. Kurosaki and S. Yamanaka, *J Alloys Compd*, 2003, 352, 48–51.

5 R. Franz and G. Wiedemann, *Ann Phys*, 1853, 165, 497–531.

6 J. Santana-Andreo, A. M. Márquez, J. J. Plata, E. J. Blancas, J.-L. González-Sánchez, J. Fdez. Sanz and P. Nath, *ACS Appl Mater Interfaces*, 2024, 16, 4606–4617.